

Multi-Skyrmion Solutions for the 6th order Skyrme Model

I.Floratos* and B. Piette†

Department of Mathematical Sciences, University of Durham,
Durham DH1 3LE, UK

March 2001

Abstract

Following Marleau [1], we study an extended version of the Skyrme model to which a sixth order term has been added to the Lagrangian and we analyse some of its classical properties. We compute the multi-Skyrmion solutions numerically for up to $B = 5$ and show that they have the same symmetries as the usual Skyrmion solutions. We use the rational map ansatz introduced by Houghton et al. [2] to evaluate the energy and the radius for multi-skyrmion solutions of up to $B = 6$ for both the $SU(2)$ and $SU(3)$ models and compare these results to the ones obtained numerically. We show that the rational map ansatz works as well for the generalised model as for the pure Skyrme model.

1 Introduction

Recent mathematical developments within the area of non-perturbative methods have established the Skyrme model as the strongest candidate for an effective low energy theory of quantum chromodynamics (QCD). The model was originally proposed by T.H.R. Skyrme [3] to describe hadron interactions. However, it was mainly ignored, until it was shown [4, 5, 6] that in the large N_c limit, where N_c is the number of colours, this non-linear theory can describe the low energy limit of QCD. This revived the Skyrme model and since then significant progress has been made towards the understanding of its properties resulting to a relatively successful description of nuclear interactions.

The Skyrme model is described by an $SU(N)$ valued field $U(\vec{x}, t)$ which must satisfy the boundary condition $U \rightarrow I$ as $|\vec{x}| \rightarrow \infty$, where I is the unit matrix. This condition

*e-mail address: Ioannis.Floratos@durham.ac.uk

†e-mail address: B.M.A.G.Piette@durham.ac.uk

ensures finiteness of the energy for any field configuration and it also implies that the three dimensional Euclidean space on which the model is defined can be compactified into S^3 . As a result, the Skyrme field U corresponds to mappings from S^3 into $SU(N)$. Skyrme's idea was to interpret the winding number associated with these topologically non trivial mappings as the baryon charge.

The model is described by the Lagrangian

$$\mathcal{L}_{Sk} = \frac{F_\pi^2}{16} Tr R_\mu R^\mu + \frac{1}{32a^2} Tr [R_\mu, R^\nu] [R_\nu, R^\mu] \quad (1)$$

where $R_\mu = (\partial_\mu U)U^{-1}$ is the right chiral current, $F_\pi = 189$ Mev is the pion decay constant and a is a dimensionless parameter. The first term in (1) is the non-linear σ -model and one can easily show using a scaling argument that with this term alone static solutions cannot exist. The same argument shows that one must add to the Lagrangian terms involving higher derivatives. This argument led Skyrme to add the second term, usually referred to as the Skyrme term, in (1) which is the simplest one that preserves the $SU(N)$ and Lorentz invariances.

The Skyrme model can be generalised by adding terms involving higher order derivatives in the Lagrangian (1) [7, 1, 8, 9]. Doing this, one introduces extra parameters that can be tuned in to increase the quality of the Skyrme model as an effective low energy limit of QCD. For example in [7, 10] the sixth-order term was used to take into account the ω -meson interactions when computing the central Nucleon-Nucleon potential. In a different context Marleau studied the model where a large number of higher order terms were included in the Lagrangian [1, 8, 9] and where, to avoid the introduction of a large number of extra parameters, the coefficients of these extra terms were all related to the coefficient of the Skyrme model.

In this paper we will consider the simplest possible extension of the Skyrme model *i.e.* defined by the Lagrangian (1) to which we add the sixth-order term

$$\mathcal{L}_6 = c_6 Tr [R_\mu, R^\nu] [R_\nu, R^\lambda] [R_\lambda, R^\mu]. \quad (2)$$

The unknown coefficient c_6 denotes the strength of this term and will be left as a free parameter of the model. This particular choice of a sixth-order term is not accidental as it is the only term that preserves the Lorentz invariance and the $SU(N)$ symmetry of the model and leads to an equation of motion that does not involve derivatives of order higher than two. This is the term that was used in [7].

In this paper we will focus our attention on the static solutions of the extended Skyrme model and thus consider fields that do not depend on time. It is also convenient to define

the dimensionless parameter $\kappa = 192c_6F_\pi^2a^4$ and to introduce the dimensionless units $y = x\sqrt{2}/(aF_\pi)\sqrt{1 + \sqrt{1 + \kappa}}$ so that the energy of the model can be written as

$$E = -\Lambda \int d\vec{x}^3 \left(\frac{1}{2} Tr R_i^2 + \frac{1-\lambda}{16} Tr [R_i, R_j]^2 + \frac{1}{96}\lambda Tr [R_i, R_j][R_j, R_k][R_k, R_i] \right) \quad (3)$$

where $\Lambda = F_\pi/(4\sqrt{2}a)\sqrt{1 + \sqrt{1 + \kappa}}$ and $\lambda = \kappa/(1 + \sqrt{1 + \kappa})^2$. The parameter Λ is the energy scale of the model. In what follows it will be convenient to use the dimensionless energy expressed in the so-called topological units *i.e.*

$$\tilde{E} = \frac{E}{12\pi^2\Lambda}. \quad (4)$$

We have chosen this parametrisation of the model so that $\lambda \in [0, 1]$ describes the mixing between the Skyrme term and the sixth-order term (2). When $\lambda = 0$ our model reduces to the usual pure Skyrme model while when $\lambda = 1$ the Skyrme term vanishes and the model reduces to what we refer to in what follows as the pure Sk6 model.

The Euler-Lagrange equations derived from (3) for the static solutions are given by

$$\partial_i \left(R_i - \frac{1}{4}(1-\lambda)[R_j, [R_j, R_i]] - \frac{1}{16}\lambda[R_j, [R_j, R_k][R_k, R_i]] \right) = 0. \quad (5)$$

As mentioned above, an important property of the Skyrme model is that its field corresponds to a mapping from S^3 into $SU(N)$ and as $\pi_3(SU(N)) = \mathbb{Z}$ each configuration is characterised by a an integer which can be obtained explicitly by evaluating the expression

$$B = \frac{1}{24\pi^2} \int_{R^3} d\vec{x}^3 \varepsilon^{ijk} Tr(R_i R_j R_k), \quad (6)$$

which following Skyrme's idea is interpreted as the baryon number. Moreover the following inequality holds for every configuration

$$\tilde{E} \geq \sqrt{1 - \lambda}B. \quad (7)$$

Our extended Skyrme model depends on three parameters: F_π , a and c_6 or using the dimensionless units, Λ , k and λ . To determine the physical values for these parameters, we can evaluate different quantities. As our analysis will be purely classical, we will use for this purpose the total energy (3) and the isoscalar mean square matter radius given by [11]

$$R^2 \equiv \langle r^2 \rangle_{I=0} = \frac{\int_0^\infty dr r^2 \rho_B(r)}{\int_0^\infty dr \rho_B(r)} \quad (8)$$

where

$$\rho_B(r) = 4\pi r^2 B^0(r). \quad (9)$$

Notice that after performing the scaling $x \rightarrow x\sqrt{2}/(aF_\pi)\sqrt{1+\sqrt{1+\kappa}}$ we can define the matter radius evaluated in dimensionless units as

$$\tilde{R} = \frac{1}{\sqrt{2}\sqrt{1+\sqrt{1+\kappa}}} aF_\pi R. \quad (10)$$

One can see from the definition of \tilde{E} and \tilde{R} that the ratio of energy or matter radius for different solutions only depends on λ . In the following section we will evaluate the energy and radius of multi-Skyrmion solutions for the general model and evaluate these two quantities with the corresponding value for the single Skyrmion and compare them directly to the experimental ratio:

$$\frac{E_B}{E_{B=1}} = \frac{\tilde{E}_B(\lambda)}{\tilde{E}_{B=1}(\lambda)} \quad \frac{R_B}{R_{B=1}} = \frac{\tilde{R}_B(\lambda)}{\tilde{R}_{B=1}(\lambda)}. \quad (11)$$

So far all the studies of the classical properties of generalised Skyrme models have been focusing on the properties of the single skyrmion ($B = 1$) [10, 7, 1, 8, 9]. In section 2 we compute numerically multi-skyrmion configurations for $B = 2$ to 5 and compare the energy and the radius of these solutions with the experimental values.

It was shown recently[2, 12] that multi-skyrmion configurations, *ie* $B \geq 2$, can be studied systematically using as an approximation the so-called harmonic map ansatz. In section 3 we approximate the multi-Skyrmion solution both for the $SU(2)$ and $SU(3)$ model using this ansatz. We compare the results obtained with the numerical solutions and we show that the harmonic map ansatz provides a good approximation for the multi-Skyrmion solutions of the extended model as well.

2 Numerical Solutions

In this section we investigate the multi-Skyrmion solutions of the extended $SU(2)$ Skyrme model by solving the static Euler-Lagrange equation (5) of the model numerically. Computing the static solutions of such a three-dimensional model is rather difficult and requires a large amount of computing power. As one has to be very careful when assessing the accuracy of such numerical results, we are giving in the Appendix a discussion of the numerical methods that we have used.

To compute the solution numerically, it is more convenient to describe the $SU(2)$ fields using a four-component vector ϕ of unit length, $|\phi|^2 = 1$, which is related to the unitary

field by $U = \phi_0 I + i \vec{\tau} \cdot \vec{\phi}$ where I is the unit matrix and $\vec{\tau}$ are the Pauli matrices. The expression for the energy (4) then becomes

$$\begin{aligned} \tilde{E} = & \frac{1}{12\pi^2} \int_R |\phi_\mu|^2 + \frac{1-\lambda}{2} \left[|\phi_\mu|^4 - (\phi_\mu \cdot \phi_\nu)^2 \right] \\ & + \frac{\lambda}{6} \left[|\phi_\mu|^6 - 3|\phi_\mu|^2 (\phi_\nu \cdot \phi_\kappa)^2 + 2(\phi_\mu \cdot \phi_\nu)(\phi_\kappa \cdot \phi_\mu)(\phi_\nu \cdot \phi_\kappa) \right], \end{aligned} \quad (12)$$

and the Euler-Lagrange equations derived from (13), after adding a Lagrange multiplier to impose the constraint $|\phi|^2 = 1$, are given by

$$\begin{aligned} & \phi_{\mu\mu} \left(1 + (1-\lambda) |\phi_\nu|^2 + \frac{1}{2}\lambda |\phi_\nu|^2 |\phi_\kappa|^2 - \frac{1}{2}\lambda (\phi_\nu \cdot \phi_\kappa)^2 \right) + |\phi_\mu|^2 \cdot \phi \\ & + (1-\lambda) \left((\phi_\nu \cdot \phi_{\nu\mu}) \phi_\mu - (\phi_{\mu\mu} \cdot \phi_\nu) \phi_\nu - (\phi_\mu \cdot \phi_\nu) \phi_{\nu\mu} + |\phi_\mu|^4 \phi - (\phi_\mu \cdot \phi_\nu)^2 \phi \right) \\ & + \lambda \left(\phi_\mu (\phi_\nu \cdot \phi_{\nu\mu}) |\phi_\kappa|^2 - \phi_\mu (\phi_\nu \cdot \phi_\kappa) (\phi_\nu \cdot \phi_{\kappa\mu}) - \phi_\nu (\phi_\mu \cdot \phi_{\mu\kappa}) (\phi_\nu \cdot \phi_\kappa) \right. \\ & \quad \left. - \phi_\nu (\phi_\nu \cdot \phi_{\kappa\kappa}) |\phi_\mu|^2 - \phi_{\nu\kappa} (\phi_\nu \cdot \phi_\kappa) |\phi_\mu|^2 + \phi_{\nu\mu} (\phi_\kappa \cdot \phi_\mu) (\phi_\nu \cdot \phi_\kappa) \right. \\ & \quad \left. + \phi_\nu (\phi_\kappa \cdot \phi_{\mu\mu}) (\phi_\nu \cdot \phi_\kappa) + \phi_\nu (\phi_\kappa \cdot \phi_\mu) (\phi_\nu \cdot \phi_{\kappa\mu}) \right. \\ & \quad \left. + \frac{1}{2} \left[|\phi_\mu|^6 - 3|\phi_\mu|^2 (\phi_\nu \cdot \phi_\kappa)^2 + 2(\phi_\mu \cdot \phi_\nu)(\phi_\kappa \cdot \phi_\mu)(\phi_\nu \cdot \phi_\kappa) \right] \phi \right) = 0. \end{aligned} \quad (13)$$

To compute the $B = 1$ solution, we use the so-called hedgehog ansatz

$$\phi = \begin{pmatrix} \sin f(r) \sin \theta \sin(\varphi) \\ \sin f(r) \sin \theta \cos(\varphi) \\ \sin f(r) \cos \theta \\ \cos f(r) \end{pmatrix} \quad (14)$$

where r , θ and φ are the usual spherical coordinates. Plugging (14) into (12) one minimises the energy for the profile function $f(r)$ which then has to satisfy an ordinary differential equation. This is a very special case of the harmonic map ansatz discussed in the next section, so we will just say at this stage that the solutions are radially symmetric and that the λ dependence of the energy and the radius of the solutions are given on Figure 1. The fact that the energy decreases with λ is entirely due to our choice of parametrisation; the real quantities one has to look at are the energy and radius ratio (11).

As described in the Appendix, solving (13) accurately is rather difficult. For this reason the case $B = 2$ was solved differently. It is indeed well known that the usual $B = 2$ static solution is axially symmetric [13, 16, 14, 15] and we found that this is also true for the extended Skyrme model. Knowing this, we can reduce the system of equations for these solutions to a two-dimensional system by using the ansatz

$$\phi = \begin{pmatrix} \sin f \sin g \sin(2\varphi) \\ \sin f \sin g \cos(2\varphi) \\ \sin f \cos g \\ \cos f \end{pmatrix} \quad (15)$$

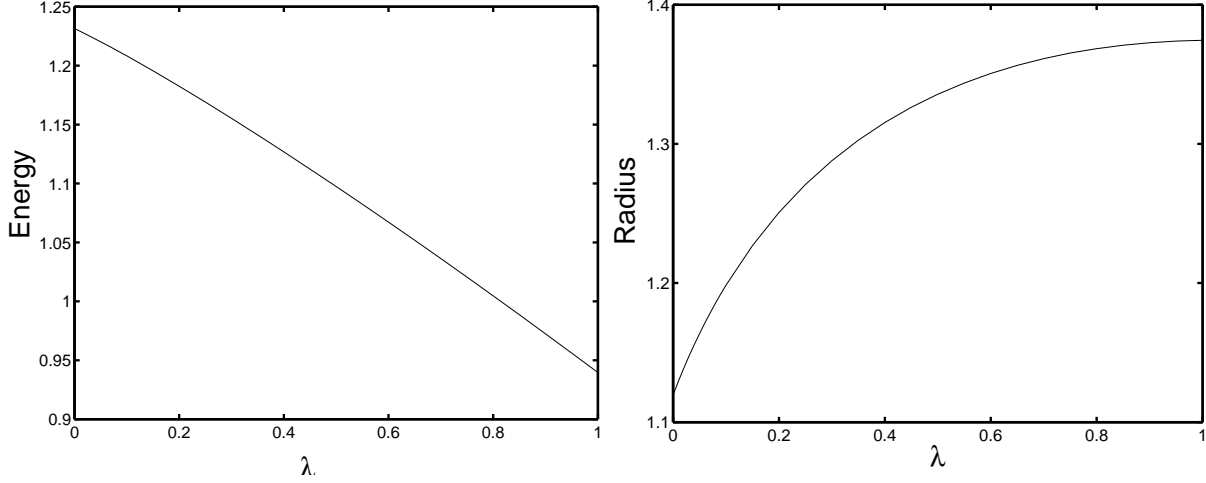


Figure 1: $\tilde{E}(\lambda)$ and $\tilde{R}(\lambda)$ for the $B = 1$ solutions.

where $\varphi = \text{atan}(y/x)$. The two profile functions, $f(\rho, z)$ and $g(\rho, z)$ are functions of the usual axial coordinates $\rho = \sqrt{x^2 + y^2}$ and z and they satisfy the following boundary conditions:

$$\begin{aligned} f(0, 0) &= \pi & f(\rho \rightarrow \infty, z \rightarrow \infty) &= 0 & f_\rho(0, z) &= 0 \\ g(0, z < 0) &= 0 & g(0, z > 0) &= \pi & g_R|_{R \rightarrow \infty} &= 0 \end{aligned} \quad (16)$$

where $R^2 = r^2 + z^2$.

Substituting (15) into (12) we get

$$\begin{aligned} E &= \frac{1}{6\pi} \int \left\{ \left[(f_\rho^2 + f_z^2) + \sin^2 f (g_\rho^2 + g_z^2) + \frac{4}{\rho^2} \sin^2 f \sin^2 g \right] \right. \\ &\quad + (1 - \lambda) \left[\frac{4}{\rho^2} \sin^2 f \sin^2 g [f_\rho^2 + f_z^2 + \sin^2 f (g_\rho^2 + g_z^2)] + \sin^2 f (f_\rho g_z - f_z g_\rho)^2 \right] \\ &\quad \left. + \lambda \left[\frac{4}{\rho^2} \sin^4 f \sin^2 g (f_\rho g_z - f_z g_\rho)^2 \right] \right\} \rho \, d\rho dz \end{aligned} \quad (17)$$

and the corresponding Euler-Lagrange equations are given by

$$\begin{aligned} &\left(f_{\rho\rho} + f_{zz} + \frac{1}{\rho} f_\rho \right) - \frac{2}{\rho^2} \sin 2f \sin^2 g - \frac{1}{2} \sin 2f (g_\rho^2 + g_z^2) \\ &+ (1 - \lambda) \left\{ \frac{4}{\rho^2} \sin^2 f \sin 2g (f_\rho g_\rho + f_z g_z) + \frac{1}{\rho} \sin^2 f (f_\rho g_z^2 - f_z g_\rho g_z) + \frac{1}{2} \sin 2f (f_\rho g_z - f_z g_\rho)^2 \right. \\ &+ \frac{4}{\rho^2} \sin^2 f \sin^2 g \left(f_{\rho\rho} + f_{zz} - \frac{1}{\rho} f_\rho \right) + \frac{4}{\rho^2} \sin 2f \sin^2 g \left[\frac{1}{2} (f_\rho^2 + f_z^2) - \sin^2 f (g_\rho^2 + g_z^2) \right] \\ &+ \sin^2 f \left\{ f_{\rho\rho} g_z^2 + f_{zz} g_\rho^2 - 2f_{z\rho} g_z g_\rho + f_\rho g_z g_{z\rho} - f_z g_{\rho\rho} g_z - f_\rho g_{zz} g_\rho + f_z g_\rho g_{\rho z} \right\} + \\ &\lambda \left\{ \frac{8}{\rho^2} \sin^2 f \sin 2f \sin^2 g (f_\rho g_z - f_z g_\rho)^2 + \frac{4}{\rho^2} \sin^4 f \sin^2 g (f_{\rho\rho} g_z^2 + f_\rho g_z g_{z\rho} - \right. \\ &- 2f_{z\rho} g_\rho g_z - f_z g_{\rho\rho} g_z + f_{zz} g_\rho^2 + f_z g_\rho g_{\rho z} - f_\rho g_{zz} g_\rho - \frac{1}{\rho} (f_\rho g_z^2 - f_z g_\rho g_z) \left. \right) - \end{aligned}$$

$$\frac{4}{\rho^2} \sin 2f \sin^2 f \sin^2 g (f_\rho g_z - f_z g_\rho)^2 \Big\} = 0 \quad (18)$$

and

$$\begin{aligned} & \left(g_{\rho\rho} + g_{zz} + \frac{1}{\rho} g_\rho \right) + \frac{\sin 2f}{\sin^2 f} (f_\rho g_\rho + f_z g_z) + \frac{2}{\rho^2} \sin 2g + (1 - \lambda) \left\{ \frac{4}{\rho^2} \sin^2 f \sin 2g (g_\rho^2 + g_z^2) + \right. \\ & \frac{4}{\rho^2} \sin^2 g \left(2 \sin 2f (f_\rho g_\rho + f_z g_z) + \sin^2 f \left(g_{\rho\rho} + g_{zz} - \frac{g_\rho}{\rho} \right) \right) + \frac{1}{\rho} (f_z^2 g_\rho - f_\rho f_z g_z) + f_z^2 g_{\rho\rho} + f_\rho^2 g_{zz} \\ & - \frac{2}{\rho^2} \sin 2g \left\{ f_\rho^2 + f_z^2 + \sin^2 f (g_\rho^2 + g_z^2) \right\} + f_z f_{z\rho} g_\rho - f_{\rho\rho} g_z f_z + f_\rho f_{\rho z} g_z - 2f_\rho g_{z\rho} f_z - f_{zz} g_\rho f_\rho \Big\} \\ & + \lambda \left\{ \frac{4}{\rho^2} \sin^2 f \sin 2g (f_z g_\rho - f_\rho g_z)^2 + \frac{4}{\rho^2} \sin^2 f \sin^2 g [f_z f_{z\rho} g_\rho + f_z^2 g_{\rho\rho} - f_{\rho\rho} f_z g_z - 2f_\rho f_z g_{z\rho} + \right. \\ & f_\rho f_{\rho z} g_z + f_\rho^2 g_{zz} - f_{zz} f_\rho g_\rho - \frac{1}{\rho} (f_z^2 g_\rho - f_\rho f_z g_z) \Big] - \frac{2}{\rho^2} \sin^2 f \sin 2g (f_\rho g_z - f_z g_\rho)^2 \Big\} = 0. \quad (19) \end{aligned}$$

The advantage of having a two-dimensional system is that we can use much larger grids and obtain much more accurate results. As discussed in the Appendix, we have also compared the $B = 2$ solutions obtained by solving (13) and (18),(19) in order to evaluate the accuracy of the method we used to solve (13) numerically.

In figures 2 to 5, we present the λ dependence of the energy and radius ratio for the $B = 2$ to $B = 5$ multi-Skyrmion solutions. We see that in each case the energy ratio decreases when the coefficient of the sixth-order term increases while on the other hand, the radius ratio increases thus making the multi-Skyrmion solution broader in all cases except for $B = 2$. Tables 1 and 2 compare the energy and radius ratio of the pure Skyrme and the pure Sk6 models with the experimental values. We notice that the predicted values for the energy are smaller than the experimental values and that the addition of the sixth-order term makes the energy ratio even smaller. On the other hand, the addition of the sixth-order term makes the multi-Skyrmion solution broader, except when $B = 2$, but the actual values are still much smaller than the experimental ones.

Another observation we made is that the symmetries of the multi-Skyrmion solutions for the general model are the same as for the pure Skyrme model. The solutions for $B = 2, 3$ and 4 Skyrmeon have respectively the shape of a torus, a tetrahedron and a cube while the $B = 5$ Skyrmeon solution has the same D_{2d} symmetry.

It is a well known problem that the binding energies predicted by the Skyrme model are too large and that the radius of the classical solutions are too small. One usually argues that quantising the model will somewhat solve this problem. Adding the sixth-order term does not improve this: the energy binding is even stronger and the multi-Skyrmion solutions are narrower except for $B=2$.

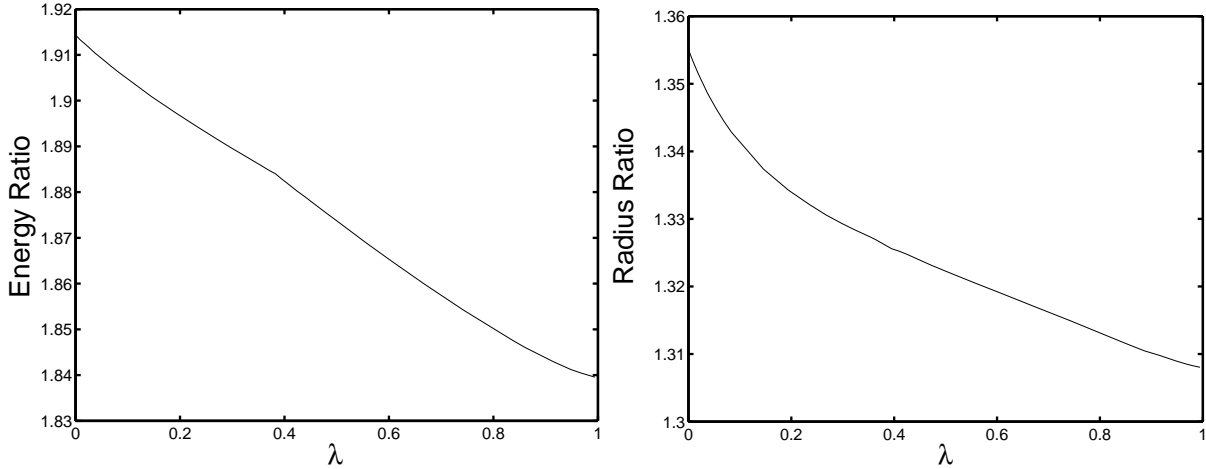


Figure 2: $\tilde{E}(\lambda)$ and $\tilde{R}(\lambda)$ ratio of $B = 2/B = 1$ for the numerical solutions.

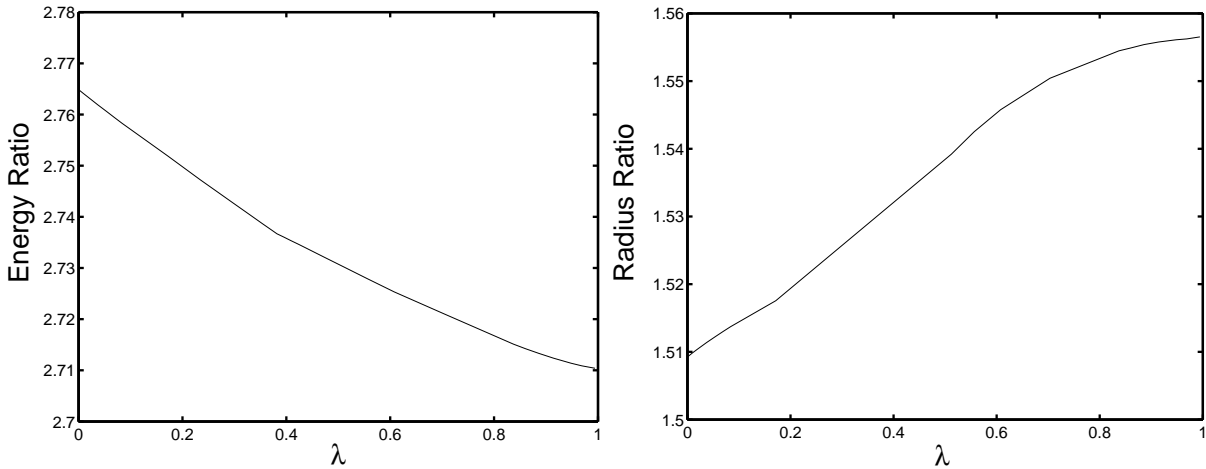


Figure 3: $\tilde{E}(\lambda)$ and $\tilde{R}(\lambda)$ ratio of $B = 3/B = 1$ for the numerical solutions.

3 Harmonic map ansatz

In this section we will use the rational map ansatz to compute configurations that approximate solutions of the extended Skyrme model. We will then use these configurations to evaluate the energy and radius of the multi-Skyrmion configurations, check how these properties depend on λ and compare these results to the ones obtained for the numerical solutions.

The rational map ansatz, introduced by Houghton et al. [2] is an extension of the

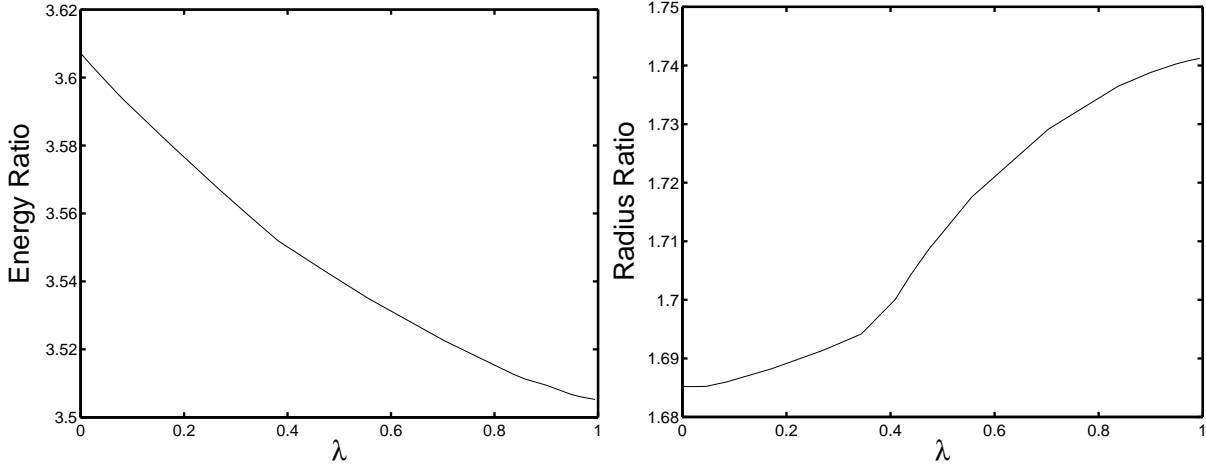


Figure 4: $\tilde{E}(\lambda)$ and $\tilde{R}(\lambda)$ ratio of $B = 4/B = 1$ for the numerical solutions.

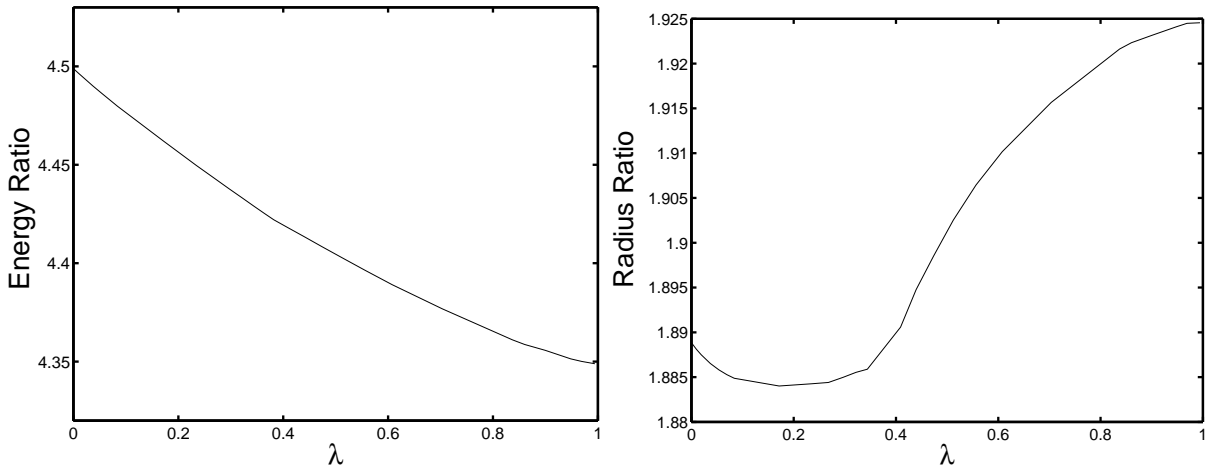


Figure 5: $\tilde{E}(\lambda)$ and $\tilde{R}(\lambda)$ ratio of $B = 5/B = 1$ for the numerical solutions.

hedgehog ansatz found by Skyrme, which using the usual polar coordinates is given by

$$U(r, \theta, \varphi) = \exp(ig(r) \hat{\mathbf{n}}(\theta, \varphi) \cdot \boldsymbol{\sigma}). \quad (20)$$

In the hedgehog ansatz \hat{n} is a unit length vector describing the one-to-one mapping of the two-sphere into itself and $g(r)$ is a profile function satisfying the boundary conditions $g(0) = \pi$ and $g(\infty) = 0$. The rational map ansatz consists in using for $\hat{n}(\theta, \varphi)$ harmonic maps from S^2 into S^2 while keeping the same boundary conditions for g . One can easily show that the baryon number for such a configuration is given by the degree of the harmonic map. To approximate a solution of a given baryon charge, one takes for \hat{n} the most general rational map of the given degree, inserts the ansatz into the expression for the energy and tries to minimise this expression with respect to the parameters of the rational map and the profile functions g . When doing so, the integration over the radius r and the angular variables θ and φ decouple and the rational map appears only in two expressions integrated over the whole sphere. One of them can be evaluated explicitly and is equal to

B	Experiment		Numerical solutions	
	Energy (MeV)	Ratio	Skyrme Ratio	Sk6 Ratio
1	939	-	-	-
2	1876.1	1.99798	1.9009	1.8395
3	2809.374	2.99188	2.7650	2.7103
4	3728.35	3.97055	3.6090	3.5045
5	4668.795	4.97209	4.5000	4.3780

Table 1: Experimental energy ratio, $E_B/E_{B=1}$, and values obtained for the numerical solutions. The experimental values (MeV) correspond to isotopes with minimum mass [17].

B	Experiment		Numerical solutions	
	Radius (fm)	Ratio	Skyrme Ratio	Sk6 Ratio
1	0.72	-	-	-
2	1.9715	2.73819	1.3549	1.308
3	1.59	2.2083	1.5080	1.5570
4	1.49	2.06944	1.6850	1.7420
5	-	-	1.8890	1.9250

Table 2: Experimental radius ratio, $R_B/R_{B=1}$ and values obtained for the numerical solutions. The experimental values (fm) correspond to nuclei with minimum mass. [11, 18, 19, 20]

the degree of the harmonic map while the other must be minimised with respect to the parameters of rational map. Doing so leads to a unique rational map, up to an arbitrary rotation, which describes the radial dependence of the Skyrmion configuration. Then one minimises the effective energy by solving the Euler-Lagrange equation for the profile function g . The configurations obtained by this construction have the same symmetries as the exact solutions [13] and their energies are only 1 or 2 percent higher [2].

This construction was later generalised by Ioannidou et al. [12] to approximate solutions of the $SU(N)$ Skyrme model using harmonic maps from S^2 into CP^{N-1} . The generalised ansatz takes the form

$$\begin{aligned}
 U(r, \theta, \varphi) &= e^{2ig(r)(P(\theta, \varphi) - I/N)} \\
 &= e^{-2ig(r)/N} \left(I + (e^{2ig(r)} - 1)P(\theta, \varphi) \right)
 \end{aligned} \tag{21}$$

where $P(\theta, \varphi)$ is an $N \times N$ projector. As we want to study some solutions of the $SU(3)$ model as well, we will use the generalised construction. At this stage it is convenient to

introduce the complex coordinate $\xi = \tan(\theta/2)e^{i\varphi}$ which corresponds to the stereographic projection of the unit sphere onto the complex plane.

The procedure to minimise the energy is the same as the one outlined above where the projector will be taken as a harmonic map from S^2 into CP^{N-1} *i.e.* a projector of the form [21]

$$P(f) = \frac{f \otimes f^\dagger}{|f|^2} \quad (22)$$

where f is a N components complex vector whose entries are all rational functions of ξ . The degree of the harmonic map is given by the highest degree of the components of f and the baryon number is again given by that degree.

Substituting the ansatz (21) in the general expression of the energy density (4) we get

$$\begin{aligned} \tilde{E} = \frac{1}{3\pi} \int dr \left(A_N g_r^2 r^2 + 2\mathcal{N} \sin^2 g (1 + (1 - \lambda)g_r^2) + (1 - \lambda)\mathcal{I} \frac{\sin^4 g}{r^2} \right. \\ \left. + \lambda \mathcal{I} \frac{\sin^4 g}{r^2} g_r^2 + \frac{2}{3} \lambda \mathcal{M} \frac{\sin^6 g}{r^4} \right) \end{aligned} \quad (23)$$

where :

$$\begin{aligned} A_N &= \frac{2}{N}(N-1), \\ \mathcal{N} &= \frac{i}{2\pi} \int d\xi d\bar{\xi} \text{Tr} (|\partial_\xi P|^2), \\ \mathcal{I} &= \frac{i}{4\pi} \int d\xi d\bar{\xi} (1 + |\xi|^2)^2 \text{Tr} ([\partial_\xi P, \partial_{\bar{\xi}} P]^2), \\ \mathcal{M} &= \frac{i}{8\pi} \int d\xi d\bar{\xi} (1 + |\xi|^2)^4 \text{Tr} ([\partial_\xi P, \partial_{\bar{\xi}} P]^3). \end{aligned} \quad (24)$$

The integral \mathcal{N} is nothing but the energy of the two-dimensional Euclidean CP^{N-1} σ -model and for the harmonic projector it is equal to the degree of the harmonic map,

$$B = \frac{i}{2\pi} \int d\xi d\bar{\xi} \text{Tr} (P [\partial_{\bar{\xi}} P, \partial_\xi P]). \quad (25)$$

As \mathcal{I} and \mathcal{M} are independent of r they can be minimised with respect to the parameters of the harmonic maps. In what follows we will prove that \mathcal{M} is identically zero so only \mathcal{I} will have to be minimised, something which was already done in [2] and [12]. The minimisation of the energy with respect to the profile function $g(r)$ is then straightforward.

To prove that \mathcal{M} vanishes, we need to use some properties of the projectors given by (22) where $\partial f / \partial \bar{\xi} = 0$. First of all, it is easy to check that

$$PP_\xi = 0 \quad \text{and} \quad P_\xi P = P_\xi \quad (26)$$

where P_ξ denotes the derivative of P with respect to ξ and from this we have

$$PP_\xi P = 0 \quad \text{and thus} \quad P_\xi^2 = 0. \quad (27)$$

Using (27) we notice that

$$\begin{aligned} \text{Tr}[P_\xi, P_\xi]^n &= \text{Tr}(P_\xi P_{\bar{\xi}} - P_{\bar{\xi}} P_\xi)^n \\ &= \text{Tr}\left((P_\xi P_{\bar{\xi}})^n + (-1)^n (P_{\bar{\xi}} P_\xi)^n\right) \\ &= (1 - (-1)^n) \text{Tr}\left((P_\xi P_{\bar{\xi}})^n\right) \end{aligned} \quad (28)$$

proving that

$$\text{Tr}[P_\xi, P_{\bar{\xi}}]^n = 0 \quad \text{for} \quad n \quad \text{odd}, \quad (29)$$

and thus that \mathcal{M} in (24) is identically zero.

As a result, the energy density (23) simplifies further and if we treat \mathcal{N} and \mathcal{I} as two parameters then one can minimise the energy \tilde{E} by solving the following Euler-Lagrange equations for g

$$\begin{aligned} g_{rr} \left(1 + 2\mathcal{N} \frac{1-\lambda}{A_N} \frac{\sin^2 g}{r^2} + \mathcal{I} \frac{\lambda}{A_N} \frac{\sin^4 g}{r^4} \right) + \frac{2}{r} g_r \left(1 - \mathcal{I} \frac{\lambda}{A_N} \frac{\sin^4 g}{r^4} \right) \\ + \frac{1}{A_N} \frac{\sin 2g}{r^2} \left(\mathcal{N} ((1-\lambda))g_r^2 - 1 \right) + \mathcal{I} \frac{\sin^2 g}{r^2} (\lambda g_r^2 - 1 + \lambda) = 0. \end{aligned} \quad (30)$$

We see from our analysis that the harmonic maps for the extended Skyrme model are the same one as the usual Skyrme model. The harmonic map ansatz predicts thus that the solutions of the usual and the extended Skyrme models have the same symmetries. This has been confirmed by the numerical solutions. The only difference, for the ansatz, between the two models comes from the profile function. This is due to the presence of the extra terms appearing in (30).

In Table 1 we list the minimum energy for the harmonic maps that we will use later together with the corresponding value for \mathcal{I} .

3.1 Energy and radius ratios for the $SU(2)$ model

In this section, we analyse how the properties of the multi-Skyrmions rational map ansatz depend on the parameter λ . Using the value of \mathcal{I} given in Table 1, we compute the profile g by solving (30) and evaluate both the total energy and the radius of the configurations.

	$SU(2)$		$SU(3)$	
B	Harmonic Map $f(\xi)$	\mathcal{I}	Harmonic Map $f(\xi)$	\mathcal{I}
1	$(\xi, 1)^t$	1	$(\xi, 1)^t$	1
2	$(\xi^2, 1)^t$	5.81	$(\xi^2, \sqrt{2}\xi, 1)^t$	4
3	$(\xi(\xi^2 - \sqrt{3}i), \sqrt{3}i\xi^2 - 1)^t$	13.58	$(\xi^3, 1.576\xi, \sqrt{2}^{-1})^t$	10.65
4	$(\xi^4 + 2\sqrt{3}i\xi^2 + 1, \xi^4 - 2\sqrt{3}i\xi^2 + 1)^t$	20.65	$(\xi^4, 2.7191\xi^2, 1)^t$	18.05
5	$(\xi(\xi^4 + b\xi^2 + a), a\xi^4 - b\xi^2 + 1)^t, a = 3.07, b = 3.94$	37.75	$(\xi^5 - 2.7\xi, 2\xi^4 + 1, 9/2\xi^3)^t$	27.26
5^*	$(\xi(\xi^4 - 5), -5\xi^4 + 1)^t$	52.05		
5^{**}			$(\xi^5, 1)^t$	84.425

Table 3: Harmonic maps $f(\xi)$ minimising the angular integral \mathcal{I} for $SU(2)$ [2] and $SU(3)$ [12]. The 5^* and 5^{**} configurations denote saddle points that we also consider.

In Figures 6 to 9, we show the energy ratio and the radius ratio defined in (11) for different values of the baryon number. At this stage we would like to remind the reader that $\lambda = 0$ corresponds to the pure Skyrme model while $\lambda = 1$ is equivalent to the pure Sk6 model. Moreover, the ratio presented on the figures only depends on λ *i.e.* the mixing between the two Skyrme terms. When $B \geq 6$, the graphs we obtained were all similar to Figure 5.

When comparing these results with the numerical solutions, we notice first of all that the energy ratio predicted by the ansatz is always too large. Apart from this, the prediction for the energy is rather good except for the case $B = 2$ where the energy difference between the numerical solution and the rational map ansatz is 7 times as large for the Sk6 model than for the pure Skyrme model.

We also notice that the graphics obtained for the numerical solutions do not exhibit local minima as observed on the graphs obtained for the harmonic map ansatz. The only exception is the radius ratio obtained for the $B = 5$ exact solution but the effect is so small that it could be a numerical artefact.

The radius ratio obtained with the harmonic map ansatz is always too large when compared with the radius ratio of the exact solution. For $B = 2$, the radius ratio increases with λ and the error only gets worse as λ increases. The case $B = 3$ is rather surprising as the radius ratio has a deep local minimum around the value $\lambda = 0.3$; this is where the relative error is the smallest, otherwise the relative error is smaller for the pure Sk6

model than for the pure Skyrme model. The cases $B = 4$ and $B = 5$ are very similar: the radius ratios decrease when λ increases and the error for the pure Sk6 model is very small especially when $B = 4$.

We can thus conclude that the harmonic map ansatz produces good approximations to the solutions of the generalised Skyrme model and the error is in most cases smaller for the pure Sk6 model than for the pure Skyrme model, the only exception being the case $B = 2$.

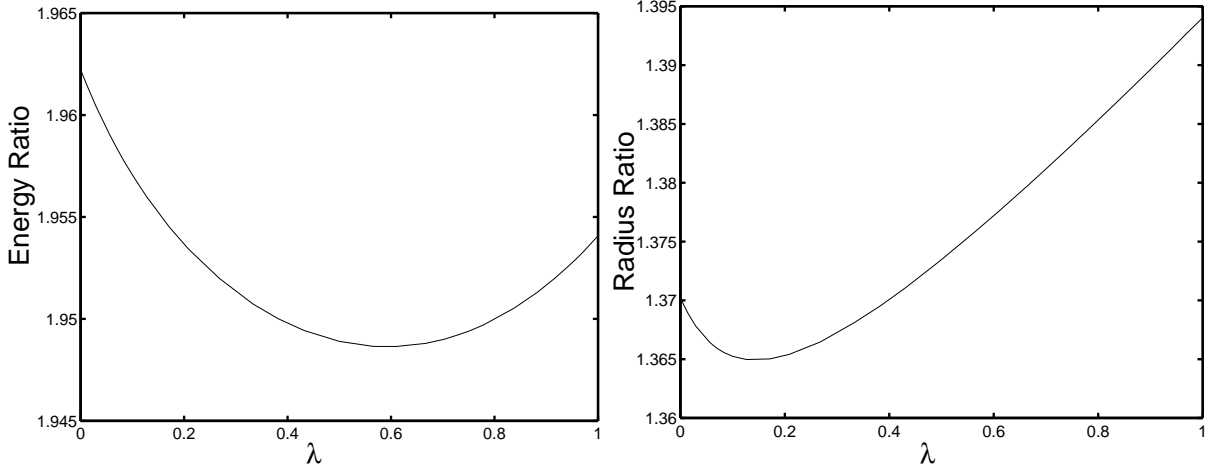


Figure 6: \tilde{E} and \tilde{R} ratio of $B = 2/B = 1$ as a function of λ .

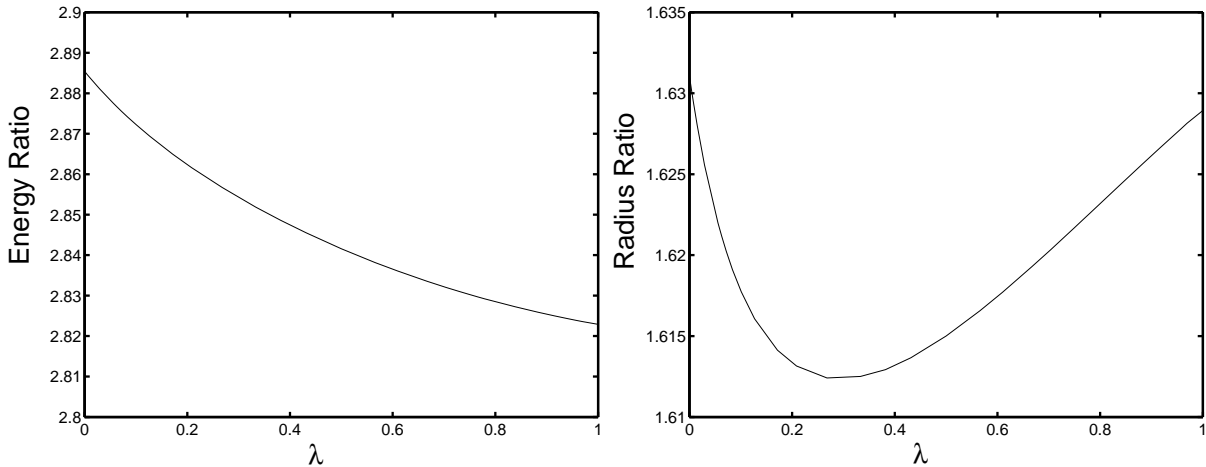


Figure 7: \tilde{E} and \tilde{R} ratio of $B = 3/B = 1$ as a function of λ .

So far we have examined the behaviour of the model for harmonic maps that minimise the angular integral \mathcal{I} and correspond to minimum energy configurations. We have next

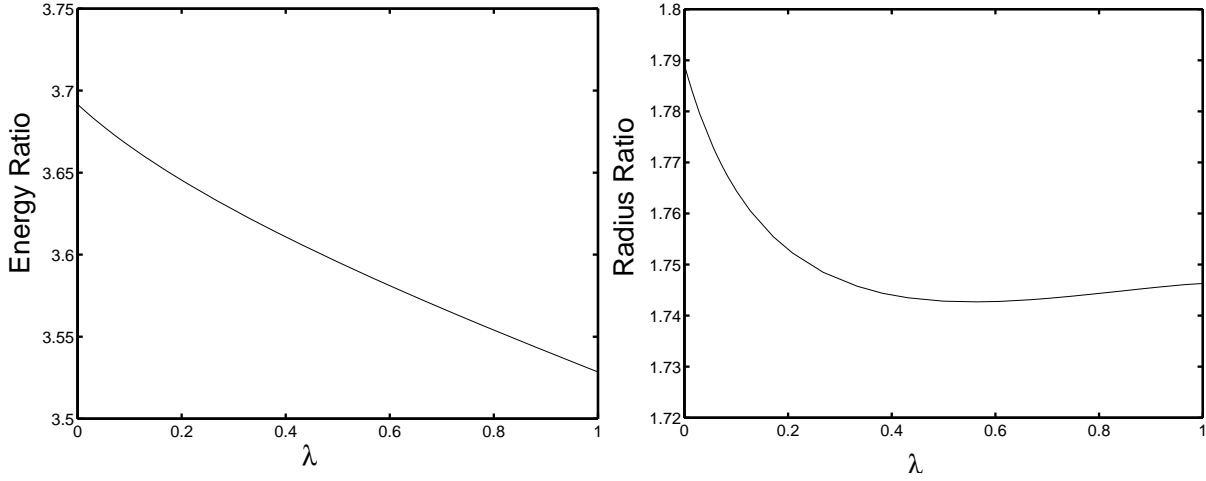


Figure 8: \tilde{E} and \tilde{R} ratio of $B = 4/B = 1$ as a function of λ .

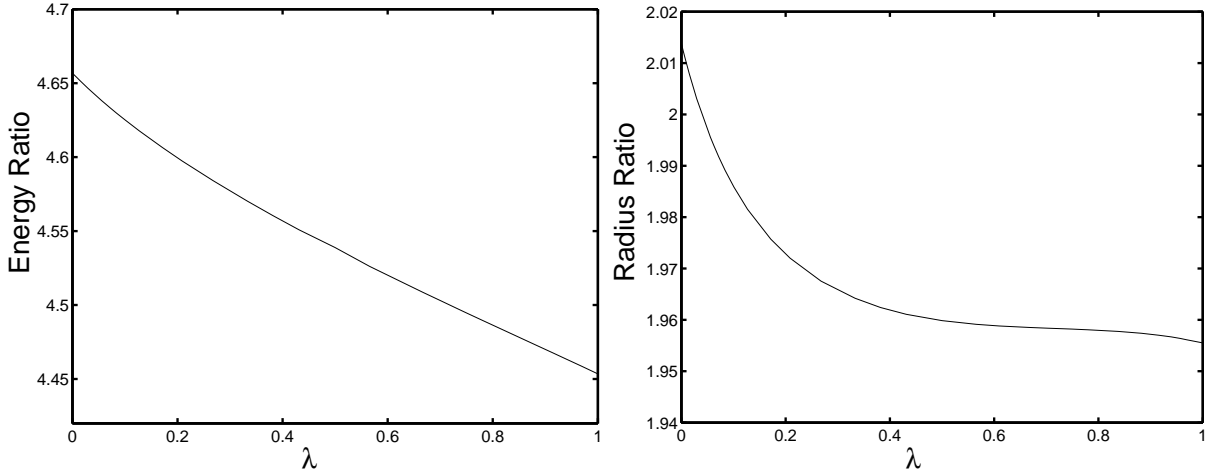


Figure 9: \tilde{E} and \tilde{R} ratio of $B = 5/B = 1$ as a function of λ .

considered harmonic maps that correspond to saddle points of the energy for $B = 5$. The reason behind this selection lies on the fact that the binding energies of the multi-Skyrmion solutions are much larger than the experimental values. For this reason, we have considered the two harmonic maps, $B = 5^*$ and $B = 5^{**}$, given in Table 3. The first one has octahedral symmetry whereas the second gives a toroidal Skyrme field [2].

For the case of $B = 5^*$, shown on Figure 10, we see that the binding energy is slightly larger than 5 for the pure Skyrme model and that it decreases when the strength of the sixth-order term increases, going through the experimental value 4.97 when $\lambda \approx 0.1$.

The second case, shown on Figure 11, is the only example where we have seen a local maxima for the energy ratio that is larger than the energy of both the pure Skyrme and Sk6 model.

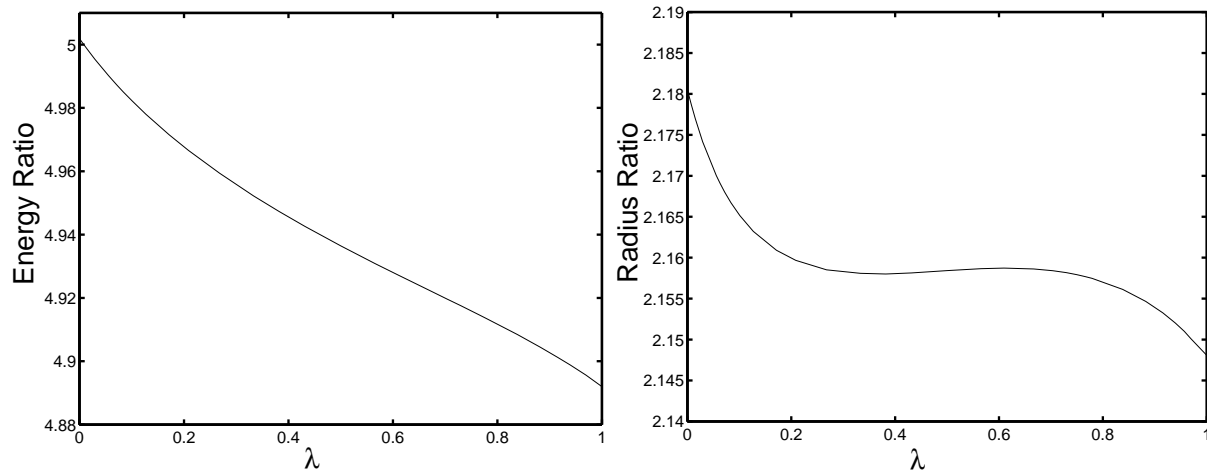


Figure 10: \tilde{E} and \tilde{R} ratio of $B = 5^*/B = 1$ as a function of λ .

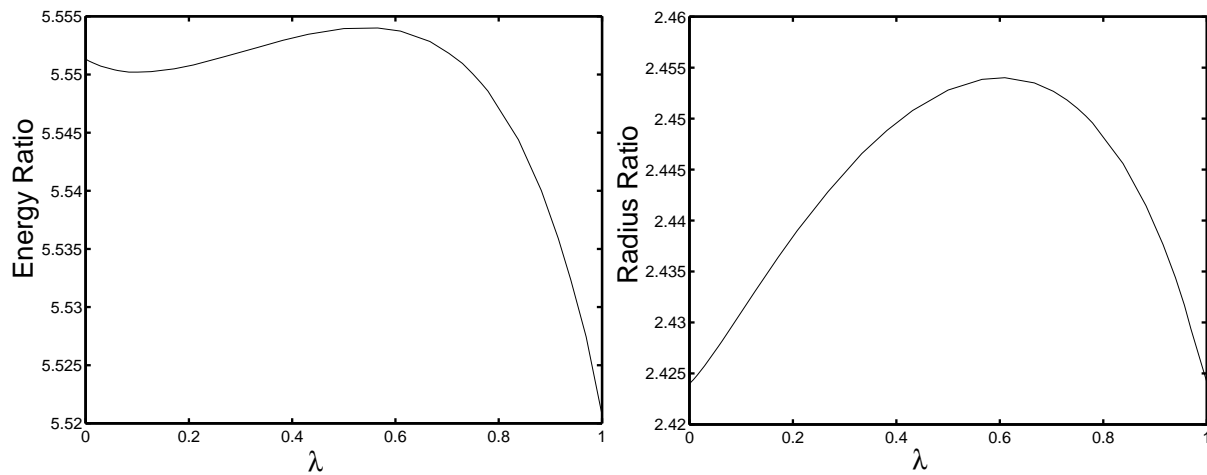


Figure 11: \tilde{E} and \tilde{R} ratio of $B = 5^{**}/B = 1$ as a function of λ .

3.2 Energy and radius ratios for the $SU(3)$ model.

In this section we look at the harmonic maps configurations for the $SU(3)$ models[12]. The harmonic maps that we will use and the corresponding values of \mathcal{I} are all given in Table 3. The single $SU(3)$ skyrmion is the well-known hedgehog ansatz and it is just an embedding of the $SU(2)$ solution.

Notice that the numerical constant A_N appearing in (30) and (23) is now equal to 4/3.

We should stress here that these configurations approximate solutions that are believed to be saddle points of the energy. Their energy is larger than the corresponding $SU(2)$ embeddings and they have a different symmetry as well.

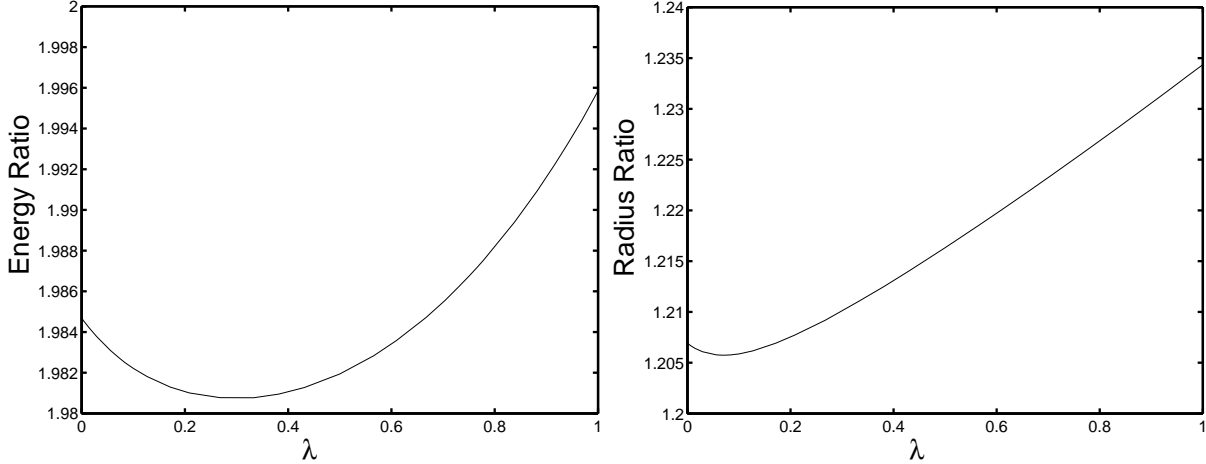


Figure 12: \tilde{E} and \tilde{R} ratio of $B = 2/B = 1$ as a function of λ for the $SU(3)$ harmonic map ansatz.

It is interesting to notice that unlike the $SU(2)$ model, the energy of the $B = 2$ solutions increases with λ . For a given B and a fixed value of λ , the energy ratio of these configurations is always larger than the energy ratio of the corresponding $SU(2)$ solutions, while on the other hand, the radius ratios is always smaller.

It is also interesting to notice that the λ dependence of the energy and radius ratios obtained for a given B looks very much like the curve obtained for the $SU(2)$ model for $B - 1$ Skyrmions. This can be explained by performing the change of variable $r \rightarrow rk$,

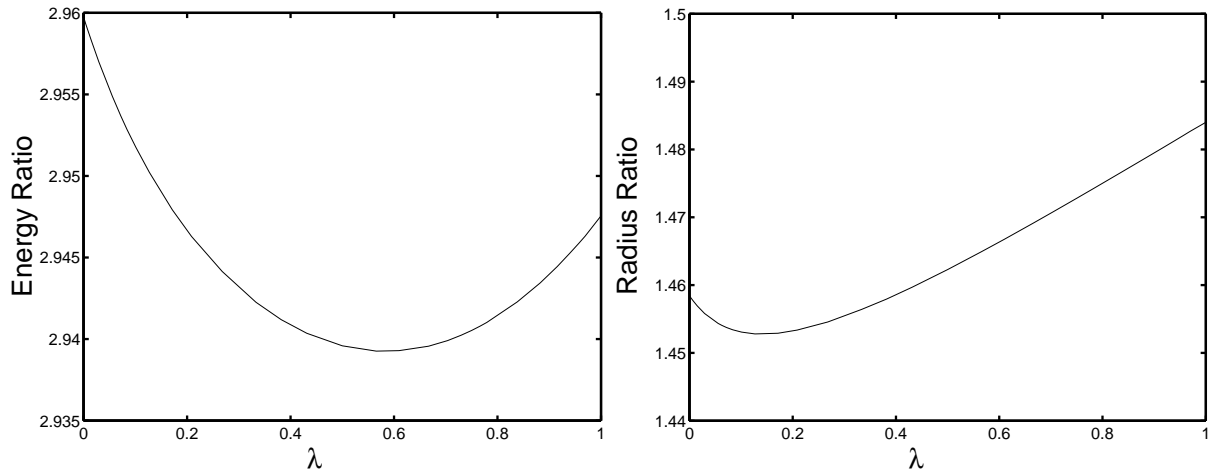


Figure 13: \tilde{E} and \tilde{R} ratio of $B = 3/B = 1$ as a function of λ for the $SU(3)$ harmonic map ansatz.

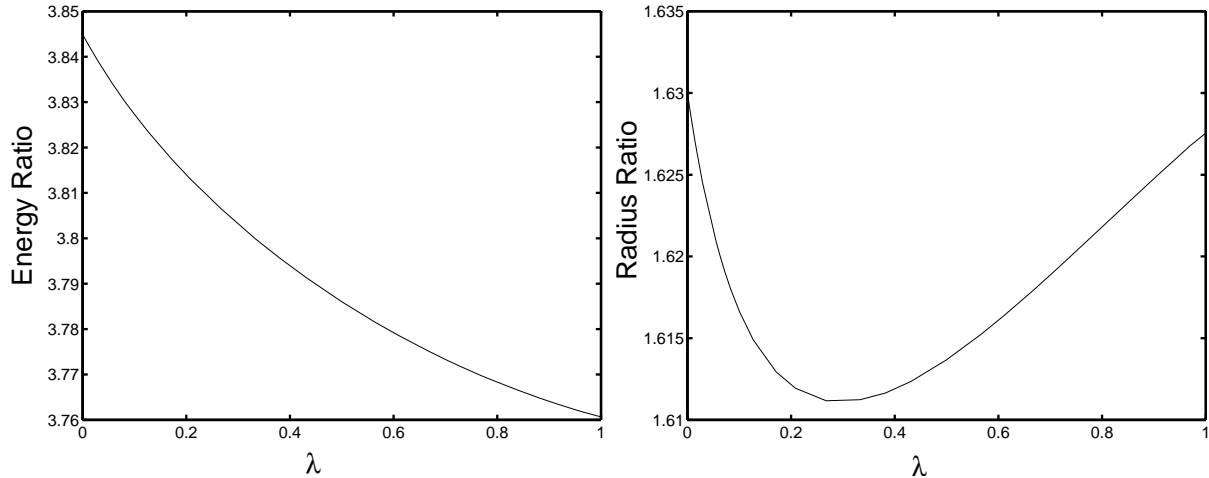


Figure 14: \tilde{E} and \tilde{R} ratio of $B = 4/B = 1$ as a function of λ for the $SU(3)$ harmonic map ansatz.

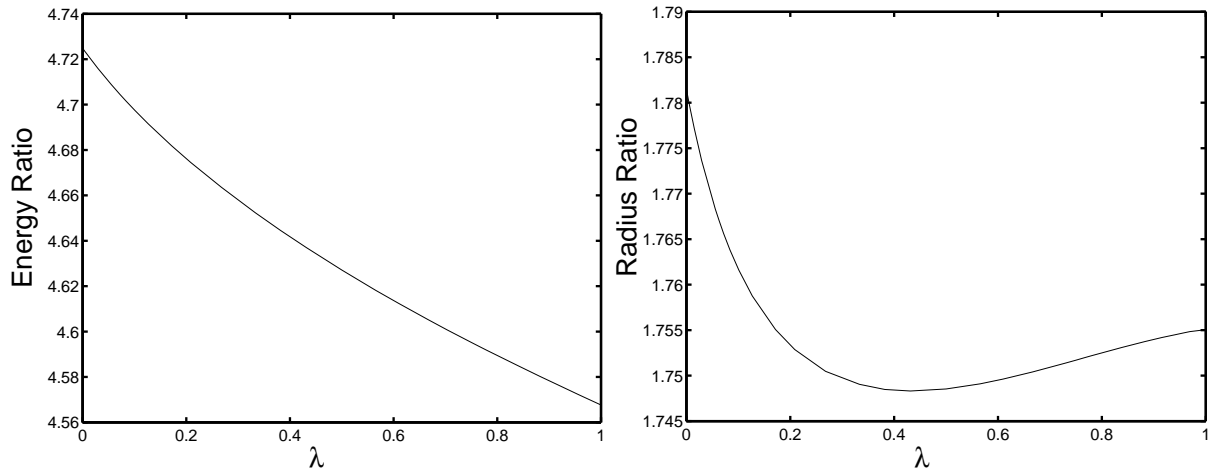


Figure 15: \tilde{E} and \tilde{R} ratio of $B = 5/B = 1$ as a function of λ for the $SU(3)$ harmonic map ansatz.

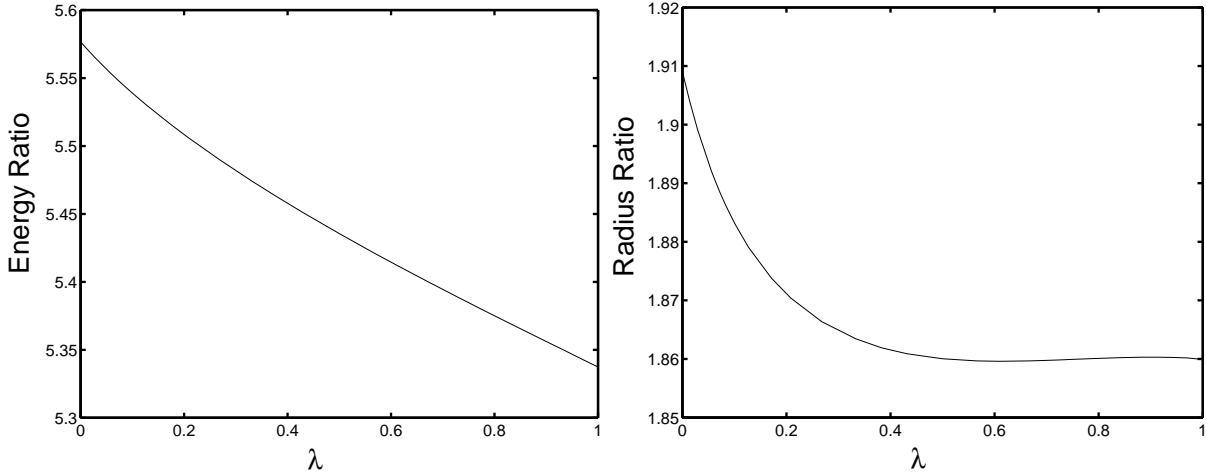


Figure 16: \tilde{E} and \tilde{R} ratio of $B = 6/B = 1$ as a function of λ for the $SU(3)$ harmonic map ansatz.

where $k^2 = \frac{(1-\lambda)}{2}(1 + \sqrt{1 + 4\lambda/(A_N(1-\lambda)^2)})$, and rewrite (23) as

$$\tilde{E} = \frac{A_N k}{3\pi} \int dr \quad (A_N g_r^2 r^2 + 2\mathcal{N}' \sin^2 g (1 + (1 - \lambda') g_r^2) + (1 - \lambda') \mathcal{I}' \frac{\sin^4 g}{k^2 r^2} + \lambda' \mathcal{I}' \frac{\sin^4 g}{r^2} g_r^2) \quad (31)$$

where $\mathcal{N}' = \mathcal{N}/A_N$, $\mathcal{I}' = \mathcal{I}/A_N$, and $\lambda' = \lambda/k^4$. The function $k(\lambda)$ monotonically decreases from $k(0) = 1$ to $k(1) = A_N^{-1/4}$ and so it is relatively close to 1 for all values of λ . In Table 4, we give the values of \mathcal{N}' and \mathcal{I}' for the $SU(3)$ ansatz and we notice that the $SU(3)$ solutions for $B = 4$ and $B = 5$ are closely related to the $SU(2)$ solutions for respectively $B = 3$ and $B = 4$.

$SU(2)$		$SU(3)$			
N	\mathcal{I}	N	\mathcal{I}	\mathcal{N}'	\mathcal{I}'
2	5.81	3	10.65	2.25	7.98
3	13.58	4	18.05	3	13.54
4	20.65	5	27.26	3.75	20.44
5	37.75	6	37.33	4.5	28

Table 4: \mathcal{N}' and \mathcal{I}' for the $SU(3)$ ansatz.

In tables 5 and 6 we compare the energies and the radius ratios, obtained for the $SU(2)$ and $SU(3)$ model using the rational map ansatz. We also compare these values with the $SU(2)$ numerical solutions.

	$SU(2)$ Numerical Solutions		$SU(2)$		$SU(3)$	
B	Skyrme Ratio	Sk6 Ratio	Skyrme Ratio	Sk6 Ratio	Skyrme Ratio	Sk6 Ratio
2	1.9009	1.8395	1.96223	1.95407	1.98468	1.99585
3	2.7650	2.7103	2.88541	2.82888	2.95974	2.94756
4	3.6090	3.5045	3.69164	3.52850	3.84491	3.76064
5	4.5000	4.3780	4.65685	4.45345	4.72485	4.56766
6	-	-	5.54105	5.26743	5.57660	5.33739

Table 5: Energy ratio, $E_B/E_{B=1}$, for the $SU(2)$ numerical solutions, and the $SU(2)$ and $SU(3)$ rational map anstaz configuration.

	$SU(2)$ Numerical Solutions		$SU(2)$		$SU(3)$	
B	Skyrme Ratio	Sk6 Ratio	Skyrme Ratio	Sk6 Ratio	Skyrme Ratio	Sk6 Ratio
2	1.3549	1.308	1.37023	1.39403	1.20691	1.234384
3	1.5080	1.5570	1.63107	1.62894	1.45842	1.483996
4	1.6850	1.7420	1.78911	1.746286	1.63002	1.62755
5	1.8890	1.9250	2.013822	1.95551	1.78149	1.75505
6	-	-	2.178298	2.09768	1.909141	1.859916

Table 6: Radius ratio, $E_B/E_{B=1}$, for the $SU(2)$ numerical solutions, and the $SU(2)$ and $SU(3)$ rational map anstaz configuration.

3.3 Conclusions

We have studied an extension of the Skyrme model defined by adding to the Lagrangian a sixth-order term. We have computed the multi-Skyrmion solutions of the extended model for up to $B = 5$ and we have shown that they have the same symmetry as the pure Skyrme model. We have analysed the dependence of the energy and radius of the classical solution with respect to the coupling constant λ . We found that the addition of the sixth-order term makes the multi-Skyrmion solution more bound than in the pure Skyrme model and that it also reduces the solution radius.

We have also used the harmonic map ansatz to approximate the numerical solutions and we found that the ansatz works as well, and in many cases even better, for the extended model than for the pure Skyrme model.

A APPENDIX

In this appendix we describe the numerical methods that we have used to compute our numerical solutions.

A.1 3 Dimensional Solutions

To compute the three dimensional solutions described in section 2, we discretised the static equations using finite differences and we solved them using the relaxation method. We used the fixed boundary condition, taking the vacuum value for the field on the edge of the grid.

The values obtained for the energy and the radius with our methods are affected by two sources of inaccuracy. The first one is the finiteness of the grid which, by distorting the field slightly, increases the value of the energy. The second one is the fact that finite differences systematically underestimate the value of the energy. One could of course hope that the two effects cancel out, but as it is difficult to evaluate their order of magnitude one has to experiment and reduce them both as much as possible.

To reduce the edge effects, we computed the same solutions on grids of different sizes L but keeping the lattice spacing $dx = L/N$ constant, where N is the number of lattice points in each direction. We then looked at how the energy changed as a function of the size and chose a value for L for which the energy is only slightly affected by the edge effects.

The finite difference scheme we used is of order two, so when we evaluate the total energy we can write

$$E = E_0 + E_1 dx + E_2 dx^2 + O(dx^3). \quad (32)$$

In theory, $E_1 = 0$ but in practice it is a small but non-zero coefficient induced by the edge effects. To improve the evaluation of the energy for a given solution, we computed the solution for at least three different values of dx using a grid of size L for which the edge effects are sufficiently small. We then fitted these values to the coefficient E_0 , E_1 and E_2 in (32) getting E_0 as a better estimation for the energy. Notice also that E_2 is always negative and that $|E_1|*dx \ll |E_2|$. When this last condition is not satisfied one must conclude that the edge effects are large and one must increase L . To check our evaluation we performed the same interpolation for the topological charge $Q = Q_0 + Q_1 dx + Q_2 dx^2 + O(dx^3)$. As

we know that it must be an integer B , the quantity $(B - Q_0)/B$ is a good estimation of the relative error on the topological charge but also on the energy E_0 .

For the solution $B = 2 \dots 5$ we used a box ranging from -8 to 8 in all directions and we used grids of 100 and 120 and 140 points. We also found that for a given value of B , E_2 did not change much with λ . We were thus able to evaluate it for a few values of λ and used an extrapolation for the other values. We also found that the relative error on the energy was smaller than 0.5% .

As an alternative method to evaluate the energy we have considered computing the quantity E/Q , as if E_2 and Q_2 were comparable, we would not have to compute the solutions for different values of dx . Unfortunately we found that with our discretisation, Q_2 is about 50% larger than E_2 and as a result the value we get for E/Q increases when dx decreases and thus underestimates the energy value.

To evaluate the radius, we have used the same method, but for this quantity the integrand decreases more slowly towards infinity and as a result the value is more affected by the finiteness of the grid. We believe that the overall behaviour of the radius ratio graph can be trusted but some of the fine details might be numerical artefacts.

To double-check our results, we have computed the $B = 2$ axially symmetric solutions by solving (18) and (19) on a two-dimensional grid. This made it possible to use many more points and much larger grids. When using the grid defined by $z \in [-20, 20]$ and $r \in [0, 20]$ taking $dx = 0.05$ the error was smaller than 0.1% and we found for example $E = 2.378$ for the pure Skyrme model. When computing this solution by solving the three-dimensional equation using the method described above, the difference between the two energies was less than 0.1% , thus validating the methods that we used.

The energy values that we obtained for the pure Skyrme model all fit within 1% the value given in [13] except for $B = 2$ where the error is 1.5% . As the numerical methods and the type of grid used are not described in [13] it is difficult to make any further comparison between the numerical results.

A.2 profiles

To compute the profile functions for the hedgehog ansatz or the harmonic map ansatz we have used both the shooting and the relaxation methods. We have in every case compared

the solutions obtained with grids of different sizes and different number of points to ensure that our results were accurate and that they were not affected by edge effects. We were led to use very large grids, $R_{max} = 80$, to get an accurate value for the radius as well as up to 160000 lattice points.

B Acknowledgement

One of us, I.F., would like to thank T. Weidig for useful discussions during the early part of this work. We would like to thank V. Piette for her linguistic advice.

References

- [1] L.Marleau, Phys. Lett. **B235**, 141 1990, **B244**, 580 1990
- [2] C. J. Houghton, N. S. Manton and P. M. Sutcliffe, Nucl. Phys. B **510**, 507 (1998).
- [3] T. H. R. Skyrme, Nucl. Phys. **31**, 556 (1962).
- [4] G.'t Hooft, Nucl. Phys. **B72**, 461 (1974)
- [5] E.Witten, Nucl. Phys. **B160**, 57 (1979)
- [6] E.Witten, Nucl. Phys. **B223** , 433 (1983)
- [7] A.Jackson, A.D.Jakson, A.S.Goldhaber,
G.S.Brown and L.C.Castillo, Phys. Lett. **B154** , 101 (1985)
- [8] L. Marleau, Phys. Rev. **D 45**, 1776 (1992)
- [9] L. Marleau, Phys. Rev. **D 63**, 036007 (2001)
- [10] G.S.Adkins and C.R.Nappi, Phys. Lett. **137B** , 251 (1984)
- [11] G.S. Adkins, C.R. Nappi and E.Witten, Nucl.Phys. **B228**, 552 (1983)
- [12] T.Ioannidou, B.Piette and W.J.Zakrzewski, J.Math.Phys. **40:6353-6365** (1999)
- [13] R.A.Battye and P. M. Sutcliffe, Phys.Rev.Lett. **79**, 363 (1997).
- [14] V.B.Kopeliovich and B.E.Stern, JETP Lett. 45 (1987) 203.
- [15] N.S.Manton, Phys. Lett. B 192 (1987) 177.

- [16] J.J.M. Verbaarschot, Phys. Lett. B 195 (1987) 235.
- [17] B.L.Cohen, *Concepts of Nuclear Physics*, McGraw Hill Series in Fundamentals of Physics, (1971)
- [18] J.Martorell, D.W.L.Sprung and D.C.Zheng, Phys. Rev. C **51**, 1127 (1995)
- [19] I.Tanihata *et al*, Phys. Lett. **B160**, 380 (1985)
- [20] P.Egelhof, Acta Physica Polonica B **30**, 487 (1999)
- [21] A. Din and W.J. Zakrzewski, Nucl. Phys. **B 174**, 397 (1980).